NANO LETTERS

pubs.acs.org/NanoLett

Letter

Controllable Synthesis of High-Quality Magnetic Topological Insulator $MnBi_2Te_4$ and $MnBi_4Te_7$ Multilayers by Chemical Vapor Deposition

Hui Guo,* Chenyu Bai, Ke Zhu, Senhao Lv, Zhaoyi Zhai, Jingyuan Qu, Guoyu Xian, Yechao Han, Guojing Hu, Qi Qi, Guangtong Liu, Fang Jiao, Lihong Bao, Xiaotian Bao, Xinfeng Liu, Hui Chen, Xiao Lin, Wu Zhou, Jiadong Zhou, Haitao Yang,* and Hong-Jun Gao

Cite This: *Nano Lett.* 2024, 24, 15788−15795

Read Online

ACCESS | Metrics & More | Article Recommendations | Supporting Information

ABSTRACT: With a nontrivial topological band and intrinsic magnetic order, two-dimensional (2D) $MnBi_2Te_4$-family materials exhibit great promise for exploring exotic quantum phenomena and potential applications. However, the synthesis of 2D $MnBi_2Te_4$-family materials via chemical vapor deposition (CVD), which is essential for advancing device applications, still remains a significant challenge since it is difficult to control the reactions among multi-precursors and form pure phases. Here, we report a controllable synthesis of high-quality magnetic topological insulator $MnBi_2Te_4$ and $MnBi_4Te_7$ multilayers via an evaporation-rate-controlled CVD approach. The multilayers are grown on a mica substrate epitaxially, exhibiting a regular triangle shape. By controlling growth temperatures, the thickness and lateral size of the 2D $MnBi_2Te_4$ are well regulated. Furthermore, the magneto-transport measurements clearly reveal multistep spin-flop transitions for both odd- and even-number-layered $MnBi_2Te_4$ multilayers. Our study marks a significant stride toward future transformative applications in devices based on high-quality, edge- and thickness-controlled 2D magnetic topological quantum materials.

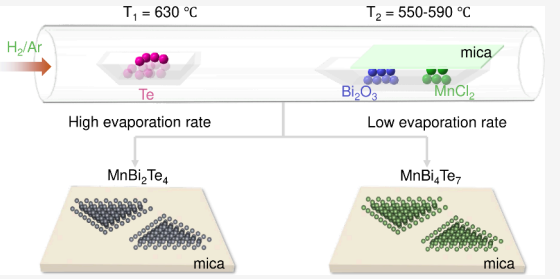

KEYWORDS: *Controllable synthesis, $MnBi_2Te_4$ multilayer, $MnBi_4Te_7$ multilayer, Chemical vapor deposition, Magnetic topological insulator*

The study of topological quantum materials has ignited considerable interest and continues to garner increased attention within the field of condensed matter research.[1−5] In particular, van der Waals (vdW) layered $MnBi_2Te_4$-family materials, $MnBi_{2n}Te_{3n+1}$ (n = 1, 2, etc.), effectively combine intrinsic magnetism and nontrivial topological band, providing exceptional platforms for exploring emergent topological states and quantum phenomena.[6−8] The $MnBi_{2n}Te_{3n+1}$ series exists with alternating $[MnBi_2Te_4]$ and $(n-1)[Bi_2Te_3]$ layers. Especially for $MnBi_2Te_4$ and $MnBi_4Te_7$, the unique magnetic structures of the ferromagnetic (FM) coupling within the layer and antiferromagnetic (AFM) coupling between the adjacent layers give rise to intriguing layer-dependent properties in their two-dimensional (2D) regime.[9−17] The 2D $MnBi_2Te_4$-family materials host a plethora of exotic phenomena including quantum anomalous Hall effect (QAHE),[9] nonlinear Hall effect,[18−20] layer Hall effect,[21] large nonreciprocal charge transport,[22] Chern/axion insulator states,[23−26] and high-Chern-number state,[27,28] to name just a few. Therefore, high-quality, uniform thickness 2D $MnBi_2Te_4$ with well-defined topography is crucial for diverse applications in topological magnetoelectric, spintronic, and dissipationless electronic devices.

However, the studies to date on 2D $MnBi_2Te_4$-family materials mainly focus on fragile and irregular nanoflakes mechanically exfoliated from the bulk, which limits the advancing device applications and integrations due to the uncontrolled, nonuniform size and thickness. To achieve the goal of a well-defined size and thickness, epitaxial growth methods such as molecular beam epitaxy[29−37] and vapor deposition have been proposed. In particular, chemical vapor deposition (CVD) has become a key method for the universal growth of high-quality atomically thin vdW materials with a well-controlled layer number and domain shape.[38−41] Due to the low cost of design, scalability to industry level, and compatibility with silicon-based technology, the CVD approach holds promise for a wider acceptance of 2D materials in future applications. However, $MnBi_{2n}Te_{3n+1}$ are ternary materials and have a series of analogous phases.[42,43] The synthesis of 2D ternary $MnBi_2Te_4$-

Received: September 22, 2024
Revised: November 19, 2024
Accepted: November 26, 2024
Published: November 28, 2024

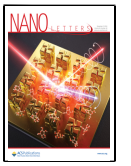

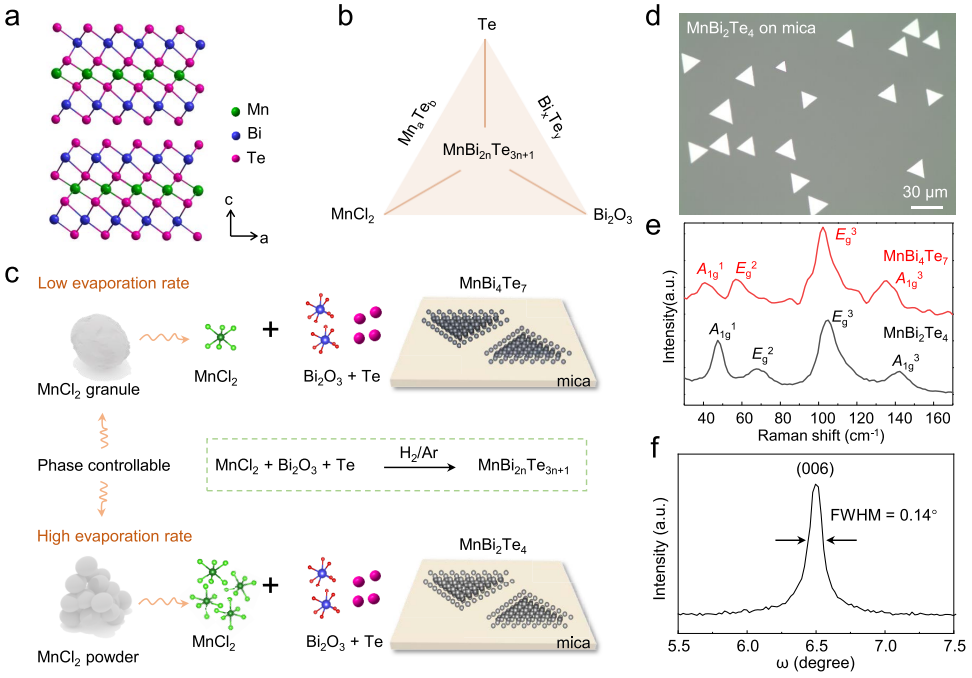

Figure 1. Controllable synthesis of high-quality triangular-shaped $MnBi_2Te_4$ and $MnBi_4Te_7$ multilayers by an evaporation-rate-controlled CVD approach. (a) Atomic structure for layered $MnBi_2Te_4$, clearly showing the SL configuration. (b) A simplified growth phase diagram of binary Mn_aTe_b, Bi_xTe_y, and ternary $MnBi_{2n}Te_{3n+1}$ family compounds. (c) Schematic of the evaporation-rate-controlled CVD process. The size of $MnCl_2$ precursors is adjusted to tune the vapor pressure and thus control the phase of the products. Utilizing the small-sized $MnCl_2$ powder produces $MnBi_2Te_4$ multilayers, while larger-sized $MnCl_2$ granules result in $MnBi_4Te_7$ multilayers. (d) An optical microscope image for the synthesized 2D $MnBi_2Te_4$ multilayer on a mica substrate, showing uniformly triangular-shaped nanosheets with lateral dimensions of a dozen micrometers. (e) Raman spectra of $MnBi_2Te_4$ (black curve) and $MnBi_4Te_7$ (red curve) multilayers for comparison, showing an obvious shift of the A_{1g}^1 and E_g^2 vibrational modes. (f) An X-ray rocking curve of (006) reflection, showing a small fwhm of 0.14°, indicating the high crystallinity of the synthesized $MnBi_2Te_4$ multilayers.

family materials via CVD still remains a substantial challenge due to the uncontrollable co-volatilization of multi-precursors and the formation of multiple phases in the resulting products.[44]

Here we report a controllable synthesis of high-quality, single-crystalline magnetic topological insulator $MnBi_2Te_4$ and $MnBi_4Te_7$ multilayers by an evaporation-rate-controlled CVD approach. We utilize a metal chloride as precursor, adjusting its size to regulate the vapor pressure and thus controlling the phases of the resulting products, i.e., formation of 2D $MnBi_2Te_4$ and $MnBi_4Te_7$ multilayers. The multilayers are grown on a mica substrate in a vdW epitaxial manner, exhibiting regular triangle shapes with tunable thicknesses and lateral sizes with increasing growth temperature. Atomic-resolution scanning transmission electron microscopy (STEM) characterizations reveal the perfect atomic structures of the $MnBi_2Te_4$ and $MnBi_4Te_7$ multilayers, indicating their high quality and single-crystalline nature. Magneto-transport measurements on both the odd- and even-number-layered 2D $MnBi_2Te_4$ show the Néel temperature of 24 K and multistep spin-flop transitions from AFM to canting AFM to FM with increasing the external magnetic fields. Our work opens up exciting prospects for future applications of a 2D intrinsic magnetic topological insulator in electronic and spintronic devices.

$MnBi_2Te_4$ has a layered tetradymite structure, which can be visualized as Bi_2Te_3 intercalated with an Mn−Te bilayer, consisting of SL stacking via vdW force (Figure 1a). The $MnBi_2Te_4$-familay materials exist with alternating $[MnBi_2Te_4]$ and $(n-1)[Bi_2Te_3]$ layers. Due to the multiple compositions and phases, the controllable synthesis of 2D $MnBi_2Te_4$-familay materials via CVD presents a significant challenge. A simplified growth phase diagram reveals the complexity of the chemical reactions among multiple precursors $MnCl_2$, Bi_2O_3, and Te during the CVD growth (Figure 1b). In principle, a suitable growth temperature for $MnBi_2Te_4$ is also thermodynamically favorable for the growth of binary compounds such as Mn_aTe_b and Bi_xTe_y, as well as other $MnBi_2Te_4$-family members such as $MnBi_4Te_7$. Therefore, precise controls on both the growth temperature and the evaporation rate are imperative for the controllable synthesis of 2D $MnBi_2Te_4$-familay materials. To overcome the challenges, we developed an evaporation-rate-controlled, halide-self-assisted CVD approach (Figure S1). We utilized $MnCl_2$ as one of the metal precursors, adjusting the grain size to regulate the evaporation rate and thus controlling the phase of the resulting products (Figure 1c). Employing small-sized $MnCl_2$ powders (about 200 μm) with a high evaporation rate yields $MnBi_2Te_4$ multilayers, while larger-sized $MnCl_2$ granules (1−2 mm) with a relatively low evaporation rate result in $MnBi_4Te_7$ multilayers.

Optical microscopy images reveal that both the $MnBi_2Te_4$ and $MnBi_4Te_7$ multilayers grown on the mica substrate exhibit regular triangular shapes with lateral sizes of a dozen micrometers (Figure 1d and Figure S2). The Raman spectrum of the $MnBi_2Te_4$ multilayers (Figure 1e) displays four well-resolved vibrational modes, A_{1g}^1 (47 cm^{-1}), E_g^2 (68 cm^{-1}), E_g^3 (104 cm^{-1}), and A_{1g}^3 (142 cm^{-1}), which is consistent with the result in the exfoliated nanoflakes,[13,45] while for the $MnBi_4Te_7$ multilayers, the A_{1g}^1 and E_g^2 vibrational modes exhibit an obvious red-shift. Energy dispersive spectrum (EDS) mappings of manganese, bismuth, and tellurium show uniform distributions, and the atomic ratio of Mn, Bi, and Te is very close to the stoichiometric ratio of $MnBi_2Te_4$ (Figure S3). Furthermore, the X-ray diffraction (XRD) pattern (Figure S4) exclusively reveals

https://doi.org/10.1021/acs.nanolett.4c04700
Nano Lett. 2024, 24, 15788−15795

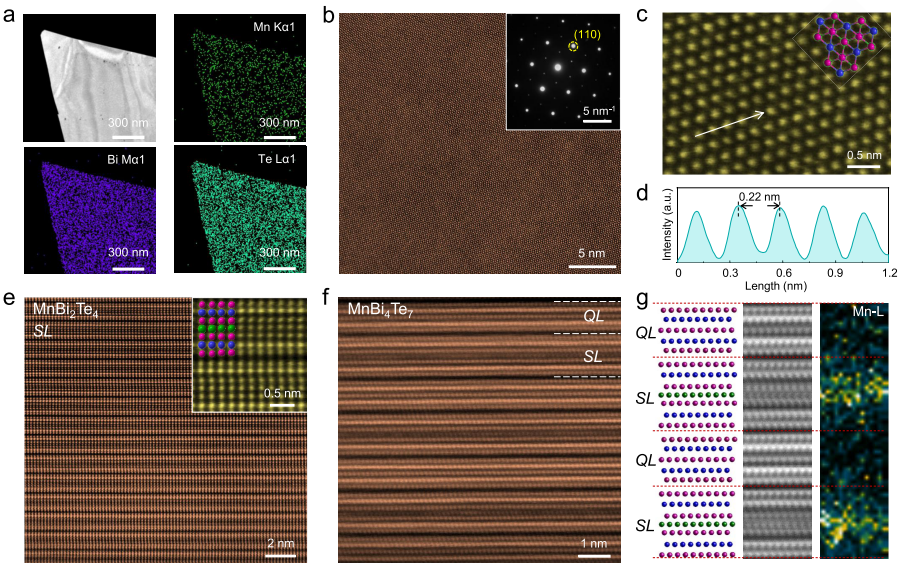

Figure 2. Atomic morphology characterizations of the synthesized 2D $MnBi_2Te_4$ and $MnBi_4Te_7$ multilayers. (a) Low-magnification TEM dark-field image of a typical $MnBi_2Te_4$ multilayer and the corresponding EDS elemental mapping for Mn, Bi, and Te, respectively, showing uniform element distributions. (b) A large-scale HAADF-STEM image observed from the [001] projection of the $MnBi_2Te_4$ multilayer and the corresponding SAED pattern (inset), showing a 3-fold rotation symmetry. (c) A close-up HAADF-STEM image, showing the atomic structure of the $MnBi_2Te_4$. Green, blue, and purple balls represent Mn, Bi, and Te atoms, respectively. (d) An intensity line profile along the white arrow in (c), showing an in-plane lattice spacing of 0.22 nm. (e) A large-scale cross-sectional STEM image for the $MnBi_2Te_4$ multilayer captured from the [1−10] projection, clearly showing the septuple-layered structure. The inset shows an enlarged cross-sectional STEM image. (f) Large-scale cross-sectional STEM image for a $MnBi_4Te_7$ multilayer, clearly showing the $MnBi_2Te_4$ SL layer separated by one Bi_2Te_3 QL layer. (g) Atomic structure and HAADF image of the $MnBi_4Te_7$ crystal with the corresponding EELS mapping of the Mn element ($L_{2,3}$ edge). The red dashed lines across the vdW gaps.

the (00*l*) diffraction peaks, and the rocking curve (Figure 1f) exhibits a small full width at half-maximum (fwhm) of 0.14°, indicating a high crystallinity.

The high-quality and single-crystalline nature of the 2D $MnBi_2Te_4$ and $MnBi_4Te_7$ multilayers is further validated by TEM measurements. A low-magnification TEM dark-field image of a typical $MnBi_2Te_4$ multilayer and the corresponding EDS mappings for Mn, Bi, and Te reveal uniform distributions of all three elements (Figure 2a). A large-area HAADF-STEM image along the [001] direction of $MnBi_2Te_4$ exhibits a pristine hexagonal lattice (Figure 2b). The corresponding selected-area electron diffraction (SAED) pattern shows sharp diffraction spots with a 3-fold rotational symmetry (inset in Figure 2b). The same set of diffraction spots collected at various locations of the $MnBi_2Te_4$ multilayer manifests its single-crystalline nature. A magnified STEM image (Figure 2c) clearly exhibits the hexagonal atomic structure of $MnBi_2Te_4$. The intensity line profile (Figure 2d) along the white arrow in Figure 2c reveals an in-plane lattice spacing of 0.22 nm, agreeing well with the (110) plane of $MnBi_2Te_4$ ($d_{(110)}$ = 0.217 nm). Moreover, the cross-sectional STEM image shows the (010) crystallographic plane of the $MnBi_2Te_4$ multilayer (Figure 2e), unambiguously revealing the resolved SL with a thickness of 1.36 nm. The relatively dark atomic layer in the middle of the SL corresponds to Mn atoms, while the two brightest layers stem from Bi atoms. The cross-sectional STEM image in Figure 2f clearly shows that one Bi_2Te_3 quintuple layer (QL) is inserted between two $MnBi_2Te_4$ SL layers in $MnBi_4Te_7$. In addition, electron energy loss spectroscopy (EELS) mapping shows Mn signals in the SL layer instead of a QL (Figure 2g). These results agree very well with the atomic structural model of $MnBi_2Te_4$ and $MnBi_4Te_7$, and there is no obvious structural defects, combined with the above macroscopic averaged measurements such as XRD, further demonstrating the high quality of the as-grown 2D $MnBi_2Te_4$ and $MnBi_4Te_7$ multilayers.

The high-quality and single-crystalline nature of the 2D $MnBi_2Te_4$ and $MnBi_4Te_7$ multilayers originates from the epitaxial growth characteristic of the mica substrate. The cleaved fluorophlogopite mica with an atomically flat and chemically inert surface has been proven to be an ideal substrate for vdW epitaxy of 2D materials without formation of interfacial chemical bonds.[46−48] Taking $MnBi_2Te_4$ as an example, a large-scale optical microscope image clearly exhibits that the triangular-shaped $MnBi_2Te_4$ multilayers predominantly grow on the terrace along two specific orientations (Figure 3a). We define the orientation angle θ, as depicted in the inset of Figure 3b, and make extensive statistical analysis in terms of $MnBi_2Te_4$ multilayers fabricated at different temperatures (Figure S5). As a result, the distribution histogram (Figure 3b) demonstrates that the $MnBi_2Te_4$ multilayers grow along two equivalent orientations, that is, aligned 0° and 60°-rotated directions, strongly indicating the vdW epitaxial growth characteristic of the 2D $MnBi_2Te_4$ multilayers on the mica substrate.

In addition to single-crystalline triangular-shaped $MnBi_2Te_4$ multilayers, polygonal $MnBi_2Te_4$ multilayers formed by merging two or more aligned triangles are achieved by increasing the coverage. Due to the vdW epitaxial growth manner, the involved triangular $MnBi_2Te_4$ multilayers tend to have parallel lattice orientations. Figure 3c shows an optical image of a polygonal $MnBi_2Te_4$ multilayer merged by two aligned triangles, labeled as A and B. High-resolution TEM images along the [001] direction and the corresponding SAED patterns taken at triangles A and B (Figure 3d−g) demonstrate that the lattice orientations of the two $MnBi_2Te_4$ triangles are identical. Moreover, SAED patterns at the junction areas of two $MnBi_2Te_4$ triangles exhibit only one set of hexagonally arranged diffraction spots (Figure S6),

https://doi.org/10.1021/acs.nanolett.4c04700
Nano Lett. 2024, 24, 15788−15795

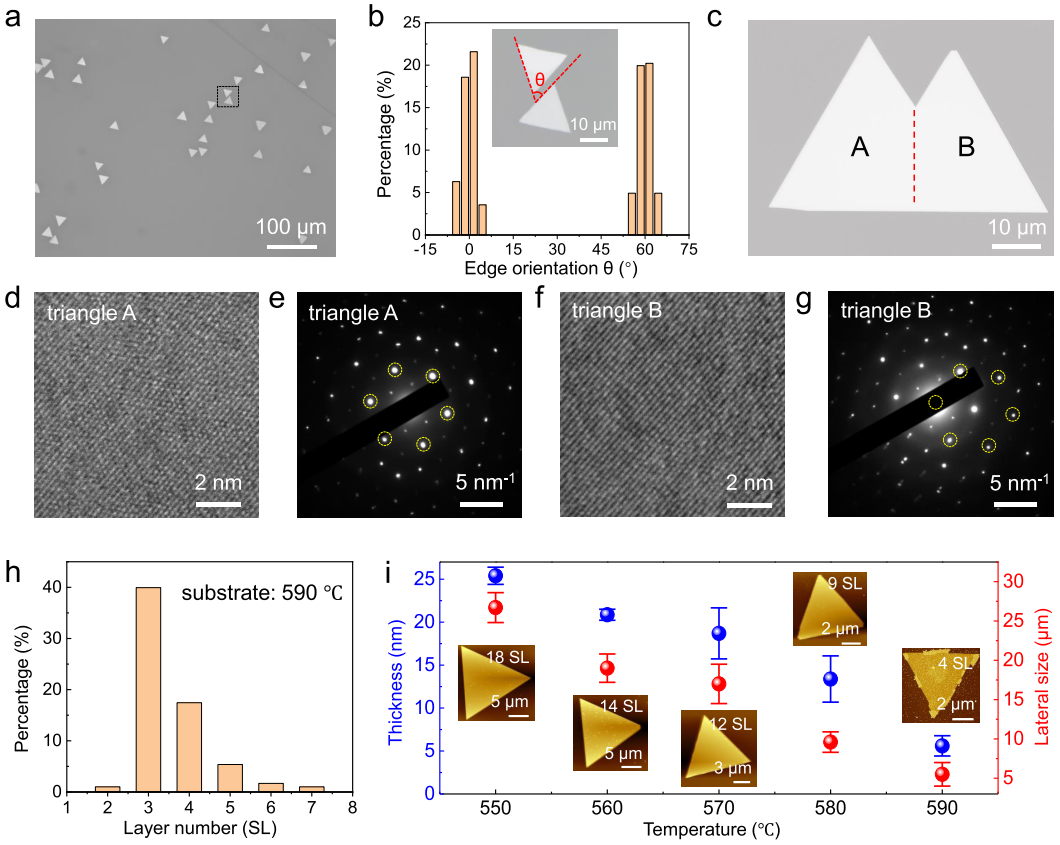

Figure 3. VdW epitaxial growth mode and evolution of thickness and lateral size for the 2D $MnBi_2Te_4$ multilayers. (a) A large-scale optical microscope image of the triangular-shaped $MnBi_2Te_4$ multilayers grown on a mica substrate at 570 °C, showing two growth orientations. (b) Statistical distribution for the growth orientations of the $MnBi_2Te_4$ multilayers, showing two almost equivalent growth orientations, indicating a vdW epitaxial growth mode for the $MnBi_2Te_4$ multilayers on the mica substrate. The inset shows the definition of the edge orientation θ according to neighboring multilayers marked by the black box in (a). (c) An optical microscope image of a polygonal $MnBi_2Te_4$ multilayer merged with two aligned triangles (A and B). (d, e) High-resolution TEM image and corresponding SAED pattern taken at triangle A, respectively. (f, g) High-resolution TEM image and corresponding SAED pattern taken at triangle B, respectively. The results show aligned lattices of $MnBi_2Te_4$ in triangles A and triangle B. (h) Statistical distribution for layer numbers of $MnBi_2Te_4$ grown at 590 °C, showing a domination of 3−4 SL. (i) Dependence of the thicknesses and lateral sizes on the growth temperature for the triangular-shaped $MnBi_2Te_4$ multilayers, showing a decrease of both thickness and lateral size with an increase in the growth temperature. Insets are typical atomic force microscopy images of the $MnBi_2Te_4$ multilayers grown at the corresponding temperatures.

indicating identical orientation of the merged triangles, which further confirms the single-crystalline nature of the polygonal $MnBi_2Te_4$ multilayers. Furthermore, with continuously increasing coverage, more $MnBi_2Te_4$ triangles can be merged to form a large-scale, single-crystalline $MnBi_2Te_4$ thin film (Figure S7), demonstrating that the epitaxial growth mode holds tremendous promise for scalability of single-crystalline $MnBi_2Te_4$ ultrathin films, offering potential for large-scale production.

We next studied the evolution of the thickness and lateral size of the $MnBi_2Te_4$ multilayers on the growth temperature. At a high substrate temperature, thermodynamics dominates the growth process, usually resulting in a thin material due to the complete precursor diffusion. The thinnest $MnBi_2Te_4$ nanosheets are achieved at a growth temperature of 590 °C. The deposition of precursors on the substrate is difficult at higher temperatures, leading to the failure to achieve a $MnBi_2Te_4$ single layer. The statistical histogram of layer numbers reveals that the $MnBi_2Te_4$ grown at 590 °C primarily consist of 3−4 SLs (Figure 3h). Figure S8 displays typical atomic force microscope images of the $MnBi_2Te_4$ multilayers with the thickness ranging from 4.7 to 8.6 nm, corresponding to three to six septuple layers, respectively. The evolution of thickness and lateral size as a function of the growth temperature (550−590 °C) is summarized in Figure 3i, demonstrating that the lateral size and thickness of the 2D single-crystalline $MnBi_2Te_4$ can be tuned by the growth temperature.

To further investigate the transport properties of the synthesized 2D $MnBi_2Te_4$ multilayers, we conduct a transfer from the mica to SiO_2/Si substrates (Figure S9a). Optical microscope images acquired before and after transfer (Figure S9b,c) reveal that the 2D $MnBi_2Te_4$ multilayers on the mica substrate can be effectively transferred to other arbitrary substrates without significant damage. Utilizing the transferred $MnBi_2Te_4$ multilayers, we proceeded to fabricate Hall bar devices by the standard electron beam lithography (EBL) technique. The insets of Figure 4a and Figure S10 show optical images of the Hall bar devices based on even-number-layered (8 SL) and odd-number-layered (11 SL) $MnBi_2Te_4$ multilayers with thicknesses of 12.2 and 15.4 nm, respectively (Figure S10a,b). The temperature-dependent longitudinal resistances ($R_{xx}-T$) of both the 8 SL and 11 SL $MnBi_2Te_4$ multilayers in the temperature range from 300 to 1.9 K distinctly exhibit an AFM transition at 24 K (Figure 4a).

To gain more insight into the magnetic structure of the $MnBi_2Te_4$ multilayers, low-temperature magnetoresistance measurements are performed under a perpendicular magnetic

https://doi.org/10.1021/acs.nanolett.4c04700
Nano Lett. 2024, 24, 15788−15795

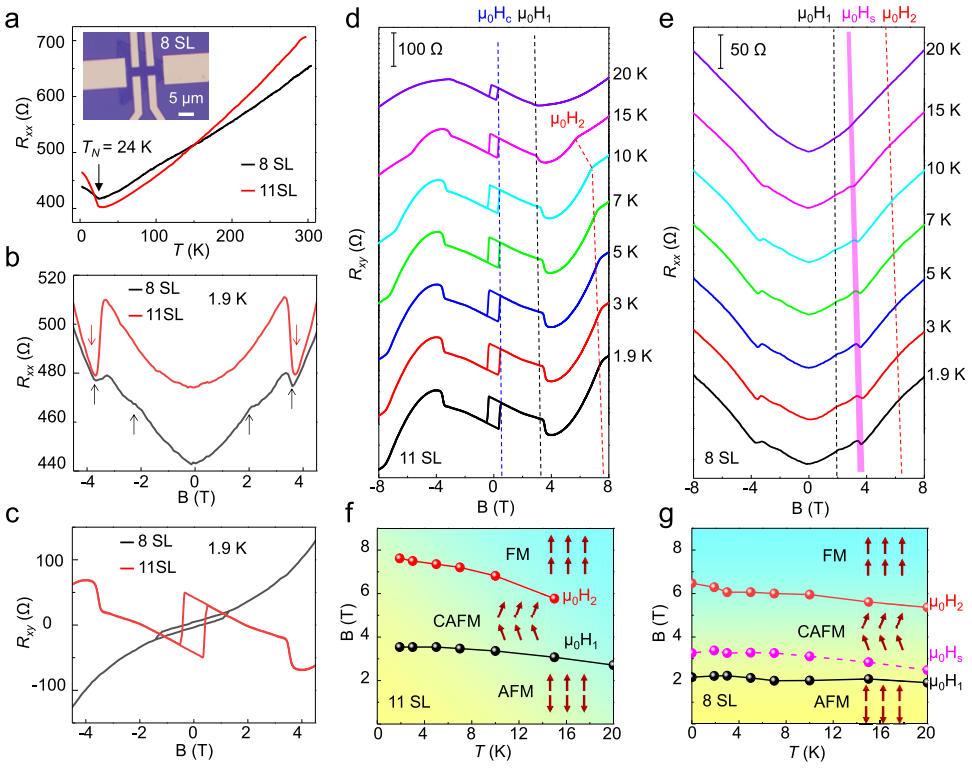

Figure 4. Multistep spin-flop transitions in both even (8 SL)- and odd (11 SL)-number-layered $MnBi_2Te_4$ multilayers. (a) Temperature-dependent R_{xx} for the 8-SL (black) and 11-SL (red) $MnBi_2Te_4$, showing an antiferromagnetic transition at 24 K. Inset shows an optical microscope image of a Hall bar device based on an 8-SL $MnBi_2Te_4$ multilayer. (b) Magnetic-field-dependent R_{xx} for the 8-SL (black) and 11-SL (red) $MnBi_2Te_4$, showing multiple transitions in the magnetoresistance curves labeled by arrows. (c) Magnetic-field-dependent Hall resistance (R_{xy}) for the 8-SL (black) and 11-SL (red) $MnBi_2Te_4$, respectively, showing an AHE in both odd- and even-number-layered samples. (d) Magnetic-field-dependent R_{xy} at various temperatures for the 11-SL $MnBi_2Te_4$. Dashed lines highlight the spin-flop transition field (μ_0H_1) and the spin-flip transition field (μ_0H_2). (e) Magnetic-field-dependent R_{xx} at various temperatures for the 8-SL $MnBi_2Te_4$. Dashed lines highlight the spin-flop transition field (μ_0H_1) and spin-flip transition field (μ_0H_2). The shaded area highlights the coherent spin rotation fields. (f, g) Magnetic phase diagrams depicting the behavior observed in 11-SL and 8-SL $MnBi_2Te_4$, respectively.

field. The magnetic-field-dependent R_{xx} at 1.9 K for both the 8-SL and 11-SL $MnBi_2Te_4$ multilayers displays several discernible transitions marked by arrows (Figure 4b). From the corresponding magnetic-field-dependent Hall resistance R_{xy} (Figure 4c), a hysteresis loop centered at 0 T can be observed for the 11-SL $MnBi_2Te_4$, indicative of an AHE, which originates from an uncompensated layer within the odd-number-layered A-type AFM material. Intriguingly, we also observe an anomalous hysteresis loop for the 8-SL $MnBi_2Te_4$, indicating a net magnetization, which is unexpected for an even-number-layered A-type AFM material. According to the previous study on the exfoliated $MnBi_2Te_4$ nanoflakes,[13] the net magnetization in 8-SL $MnBi_2Te_4$ is potentially from the surface-related magnetization attributed to the magnetic moment asymmetry of the top and bottom surfaces. The AHE values at various temperatures for 8-SL and 11-SL $MnBi_2Te_4$ are depicted in Figure S11a and Figure 4d, respectively. From the temperature dependence of the extracted coercivity μ_0H_c (Figure S11b), we find that the $\mu_0H_c^{8SL}$ (~1.3 T at 1.9 K) is much larger than $\mu_0H_c^{11SL}$ (~0.5 T at 1.9 K), which is possibly due to the fact that a higher magnetic field is required for the Zeeman energy to overcome the anisotropy energy in the 8-SL sample.[13] Besides, from the Hall measurements under high magnetic fields (Figure S11c), we can extract the carrier mobility of about 900 $cm^2\ V^{-1}\ s^{-1}$, indicating the high-quality nature of the synthesized $MnBi_2Te_4$ multilayers.

Now we focus on the spin-flop transitions for both odd- and even-number-layered $MnBi_2Te_4$ multilayers. The magnetic-field-dependent R_{xy} curves for the 11-SL $MnBi_2Te_4$ at different temperatures obviously exhibit two transitions around 3.4 T (μ_0H_1) and 7.5 T (μ_0H_2), corresponding to the beginning of a magnetic-field-driven spin-flopping process and a complete spin-flip transition, respectively (Figure 4d). Within the external magnetic field between μ_0H_1 and μ_0H_2, the $MnBi_2Te_4$ multilayer has a noncollinear spin structure, that is, a canting AFM state (CAFM). When the applied magnetic field is below μ_0H_1 or above μ_0H_2, however, the $MnBi_2Te_4$ multilayer remains in the A-type AFM state or transits to the FM state, respectively. Similarly, the spin-flop (μ_0H_1) and spin-flip (μ_0H_2) transitions can also be recognized around 2 and 6 T, respectively, from the magnetic-field-dependent R_{xx} curves for the 8-SL $MnBi_2Te_4$ at various temperatures (Figure 4e). The spin-flop transition in the 11-SL sample (3.4 T) occurs at a higher magnetic field than that in the 8-SL sample (2 T) because the magnetization of one uncompensated layer in the 11-SL sample contributes a finite Zeeman energy to the total energy under the external magnetic field at the AFM state. However, different from the 11-SL $MnBi_2Te_4$, a distinct small drop around 3 T (highlighted by μ_0H_s) is observed, which is associated with a coherent spin-rotation in a narrow magnetic-field range.[13] By carefully analyzing the R_{xx} and R_{xy} curves at various temperatures (Figures S12, S13), we extract the transition fields and plot the magnetic phase diagrams for the 11-SL and 8-SL $MnBi_2Te_4$ (Figure 4f and 4g, respectively), clearly showing the magnetic order transitions from AFM to CAFM to FM. These results

https://doi.org/10.1021/acs.nanolett.4c04700
Nano Lett. 2024, 24, 15788−15795

further indicate the high quality of the CVD-synthesized 2D $MnBi_2Te_4$ multilayers. Additionally, we attempted to modulate the AHE of the 11-SL $MnBi_2Te_4$ by applying various gate voltages (Figure S14). The results indicate some control over the Fermi level; however, significantly larger gate modulation is needed to tune the Fermi level into the band gap, potentially due to the high doping of the CVD-grown $MnBi_2Te_4$.

In summary, we have proposed an evaporation-rate-controlled CVD method and successfully realized controllable synthesis of single-crystalline, triangular-shaped 2D $MnBi_2Te_4$ and $MnBi_4Te_7$ multilayers. The high-quality and single-crystalline nature of the synthesized multilayers is evidenced by XRD and STEM characterizations. The thickness and lateral size can be controlled well by the growth temperature. Moreover, the $MnBi_2Te_4$ and $MnBi_4Te_7$ multilayers are grown on the mica substrate in a vdW epitaxial mode, offering a promise for scalability of single-crystalline ultrathin films. Notably, both even- and odd-number-layered $MnBi_2Te_4$ exhibit multiple spin-flop transitions from AFM to CAFM to FM with increasing applied magnetic field. This work opens up exciting avenues for the future development of device applications and integrations based on high-quality 2D magnetic topological quantum materials.

EXPERIMENTAL METHODS

CVD Synthesis of 2D $MnBi_2Te_4$ and $MnBi_4Te_7$ Multilayers. High-quality triangular-shaped 2D $MnBi_2Te_4$ and $MnBi_4Te_7$ multilayers were synthesized by an evaporation-rate-controlled, halide-self-assisted CVD method using a two-zone tube furnace connected to a glovebox. Tellurium lumps, $MnCl_2$ powders/granules, and Bi_2O_3 powders were used as precursors, and the cleaved mica was adopted as substrate. A quartz boat with tellurium lumps was placed in the upstream zone, and another quartz boat with $MnCl_2$ and Bi_2O_3 was placed in the downstream zone. The mica substrate was facedown above the $MnCl_2$ and Bi_2O_3 precursors. We chose $MnCl_2$ and Bi_2O_3 as the precursors due to their suitable evaporation rates within the optimal growth temperature range, allowing for a well-controlled growth of the $MnBi_2Te_4$-family materials. After purging the quartz tube with a mixture of H_2/Ar (1:9, v/v) gas for 10 min, the furnace was ramped up to 550−590 °C in 15 min with H_2/Ar carrier gas at a flow rate of 100 sccm (standard cubic centimeters per minute). After holding for 1 min, the furnace was cooled down to room temperature naturally.

Sample Characterizations. The morphology of $MnBi_2Te_4$ multilayers was characterized by an Olympus BX51-SC30 optical microscope. Raman spectra were obtained on a WITec ALPHA300R. XRD measurements were performed by a Rigaku SmartLab SE X-ray diffractometer with Cu Kα radiation. SEM images and EDS analysis were collected by a Hitachi SU5000 with a Bruker Quantax XFlash 6160. The atomic force microscope images were assembled by an OXFORD Cypher S AFM. High-resolution TEM was carried out on a JEOL JEM-2100Plus. STEM images were collected by a JEOL JEM-ARM200F.

Transfer of the 2D Multilayers. The as-grown 2D multilayers were transferred from mica to the SiO_2/Si substrate by using polystyrene (PS) as a support polymer. First, 2 g of PS particles were dissolved in 20 mL of toluene, and then the PS solution was spin-coated (3000 rpm for 60 s) on the mica substrates with the as-grown 2D multilayers on them. Subsequently, it was baked for 20 min at 60 °C followed by cutting the edge of PS/mica and putting it on the surface of water. The mica substrate was separated quickly with a PS/$MnBi_2Te_4$ film floating on the surface. After the PS/$MnBi_2Te_4$ film was successfully transferred to the SiO_2/Si substrate, it was baked for 40 min at 80 °C and the PS was dissolved in toluene.

Device Fabrication and Transport Measurements. The Hall bar devices based on $MnBi_2Te_4$ multilayers were fabricated by standard e-beam lithography (Raith 150), followed by deposition of 5/50 nm Cr/Au as electrodes using thermal evaporation. Electrical transport properties were carried out on a Quantum Design physical property measurement system (PPMS).

ASSOCIATED CONTENT

Supporting Information

The Supporting Information is available free of charge at https://pubs.acs.org/doi/10.1021/acs.nanolett.4c04700.

Additional figures (PDF)

AUTHOR INFORMATION

Corresponding Authors

Hui Guo − *Beijing National Center for Condensed Matter Physics and Institute of Physics, Chinese Academy of Sciences, Beijing 100190, PR China; School of Physical Sciences, University of Chinese Academy of Sciences, Beijing 100049, PR China*; Email: guohui@iphy.ac.cn

Haitao Yang − *Beijing National Center for Condensed Matter Physics and Institute of Physics, Chinese Academy of Sciences, Beijing 100190, PR China; School of Physical Sciences, University of Chinese Academy of Sciences, Beijing 100049, PR China*; Email: htyang@iphy.ac.cn

Authors

Chenyu Bai − *Beijing National Center for Condensed Matter Physics and Institute of Physics, Chinese Academy of Sciences, Beijing 100190, PR China; School of Physical Sciences, University of Chinese Academy of Sciences, Beijing 100049, PR China*

Ke Zhu − *Beijing National Center for Condensed Matter Physics and Institute of Physics, Chinese Academy of Sciences, Beijing 100190, PR China; School of Physical Sciences, University of Chinese Academy of Sciences, Beijing 100049, PR China*

Senhao Lv − *Beijing National Center for Condensed Matter Physics and Institute of Physics, Chinese Academy of Sciences, Beijing 100190, PR China*

Zhaoyi Zhai − *Beijing National Center for Condensed Matter Physics and Institute of Physics, Chinese Academy of Sciences, Beijing 100190, PR China; School of Physical Sciences, University of Chinese Academy of Sciences, Beijing 100049, PR China*

Jingyuan Qu − *Beijing National Center for Condensed Matter Physics and Institute of Physics, Chinese Academy of Sciences, Beijing 100190, PR China*

Guoyu Xian − *Beijing National Center for Condensed Matter Physics and Institute of Physics, Chinese Academy of Sciences, Beijing 100190, PR China; School of Physical Sciences, University of Chinese Academy of Sciences, Beijing 100049, PR China*

Yechao Han − *School of Physical Sciences, University of Chinese Academy of Sciences, Beijing 100049, PR China*

Guojing Hu − *Beijing National Center for Condensed Matter Physics and Institute of Physics, Chinese Academy of Sciences, Beijing 100190, PR China*

https://doi.org/10.1021/acs.nanolett.4c04700
Nano Lett. 2024, 24, 15788−15795

Qi Qi − *Beijing National Center for Condensed Matter Physics and Institute of Physics, Chinese Academy of Sciences, Beijing 100190, PR China; School of Physical Sciences, University of Chinese Academy of Sciences, Beijing 100049, PR China*

Guangtong Liu − *Beijing National Center for Condensed Matter Physics and Institute of Physics, Chinese Academy of Sciences, Beijing 100190, PR China; School of Physical Sciences, University of Chinese Academy of Sciences, Beijing 100049, PR China*

Fang Jiao − *Beijing National Center for Condensed Matter Physics and Institute of Physics, Chinese Academy of Sciences, Beijing 100190, PR China; School of Physical Sciences, University of Chinese Academy of Sciences, Beijing 100049, PR China;* orcid.org/0000-0001-5087-6228

Lihong Bao − *Beijing National Center for Condensed Matter Physics and Institute of Physics, Chinese Academy of Sciences, Beijing 100190, PR China; School of Physical Sciences, University of Chinese Academy of Sciences, Beijing 100049, PR China;* orcid.org/0000-0002-2942-892X

Xiaotian Bao − *CAS Key Laboratory of Standardization and Measurement for Nanotechnology, National Center for Nanoscience and Technology, Beijing 100190, PR China*

Xinfeng Liu − *CAS Key Laboratory of Standardization and Measurement for Nanotechnology, National Center for Nanoscience and Technology, Beijing 100190, PR China;* orcid.org/0000-0002-7662-7171

Hui Chen − *Beijing National Center for Condensed Matter Physics and Institute of Physics, Chinese Academy of Sciences, Beijing 100190, PR China; School of Physical Sciences, University of Chinese Academy of Sciences, Beijing 100049, PR China;* orcid.org/0000-0002-3369-8113

Xiao Lin − *School of Physical Sciences, University of Chinese Academy of Sciences, Beijing 100049, PR China;* orcid.org/0000-0002-2490-4691

Wu Zhou − *School of Physical Sciences, University of Chinese Academy of Sciences, Beijing 100049, PR China*

Jiadong Zhou − *Key Laboratory of Advanced Optoelectronic Quantum Architecture and Measurement, School of Physics, Beijing Institute of Technology, Beijing 100081, PR China;* orcid.org/0000-0001-5268-2136

Hong-Jun Gao − *Beijing National Center for Condensed Matter Physics and Institute of Physics, Chinese Academy of Sciences, Beijing 100190, PR China; School of Physical Sciences, University of Chinese Academy of Sciences, Beijing 100049, PR China;* orcid.org/0000-0002-6766-0623

Complete contact information is available at: https://pubs.acs.org/10.1021/acs.nanolett.4c04700

Author Contributions

H.G. and C.B. contributed equally to this work.

Author Contributions

H.-J.G. and H.T.Y. supervised and coordinated the research project. H.G., C.Y.B., and J.D.Z. synthesized the materials. H.G., C.Y.B., G.Y.X., Z.Y.Z., Q.Q., F.J., X.T.Y., X.F.L., H.C., X.L., and W.Z. performed the structural characterizations. H.G., S.H.L., K.Z., Y.C.H., G.J.H., L.H.B., and G.T.L. performed the device fabrication and transport measurements. All of the authors participated in analyzing the experimental data, plotting figures, and writing the manuscript.

Notes

The authors declare no competing financial interest.

■ ACKNOWLEDGMENTS

We thank Dr. Yang Xu and Dr. Miaoling Lin for their helpful discussions. This work was supported by the National Key Research and Development Projects of China (2022YFA1204100), the National Natural Science Foundation of China (62488201, 52072401), the Chinese Academy of Sciences (XDB33030100), the CAS Project for Young Scientists in Basic Research (YSBR-053, YSBR-003), and Innovation Program of Quantum Science and Technology (2021ZD0302700).

■ REFERENCES

(1) Hasan, M. Z.; Kane, C. L. Colloquium: topological insulators. *Rev. Mod. Phys.* **2010**, *82*, 3045−3067.

(2) Tokura, Y.; Yasuda, K.; Tsukazaki, A. Magnetic topological insulators. *Nat. Rev. Phys.* **2019**, *1*, 126−143.

(3) Yin, J.-X.; Pan, S. H.; Hasan, M. Z. Probing topological quantum matter with scanning tunnelling microscopy. *Nat. Rev. Phys.* **2021**, *3*, 249−263.

(4) Qi, X.-L.; Zhang, S.-C. Topological insulators and superconductors. *Rev. Mod. Phys.* **2011**, *83*, 1057−1110.

(5) Chang, C.-Z.; Zhang, J.; Feng, X.; Shen, J.; Zhang, Z.; Guo, M.; Li, K.; Ou, Y.; Wei, P.; Wang, L.-L.; Ji, Z. Q.; Feng, Y.; Ji, S.; Jia, J.; Dai, X.; Fang, Z.; Zhang, S.-C.; He, K.; Wang, Y.; Lv, L.; Ma, X.; Xue, Q.-K. Experimental observation of the quantum anomalous Hall effect in a magnetic topological insulator. *Science* **2013**, *340*, 167−170.

(6) Li, S.; Liu, T.; Liu, C.; Wang, Y.; Lu, H.-Z.; Xie, X. C. Progress on the antiferromagnetic topological insulator $MnBi_2Te_4$. *Natl. Sci. Rev.* **2024**, *11*, No. nwac296.

(7) Tan, W.; Liu, J.; Li, H.; Guan, D.; Jia, J.-F. $MnBi_2Te_4$ − a good platform for topological quantum physics study. *Quantum Front.* **2022**, *1*, 19.

(8) Padmanabhan, H.; Stoica, V. A.; Kim, P. K.; Poore, M.; Yang, T.; Shen, X.; Reid, A. H.; Lin, M.-F.; Park, S.; Yang, J.; Wang, H.; Koocher, N.; Pugginoi, D.; Georgescu, A.; Min, L.; Lee, S.; Mao, Z.; Rondinelli, J.; Lindenberg, A.; Chen, L.-Q.; Wang, X.; Averitt, R.; Freeland, J.; Gopalan, V. Large exchange coupling between localized spins and topological bands in $MnBi_2Te_4$. *Adv. Mater.* **2022**, *34*, No. 2202841.

(9) Deng, Y.; Yu, Y.; Shi, M. Z.; Guo, Z.; Xu, Z.; Wang, J.; Chen, X. H.; Zhang, Y. Quantum anomalous Hall effect in intrinsic magnetic topological insulator $MnBi_2Te_4$. *Science* **2020**, *367*, 895−900.

(10) Li, J.; Li, Y.; Du, S.; Wang, Z.; Gu, B.-L.; Zhang, S.-C.; He, K.; Duan, W.; Xu, Y. Intrinsic magnetic topological insulators in van der Waals layered $MnBi_2Te_4$-family materials. *Sci. Adv.* **2019**, *5*, No. eaaw5685.

(11) Otrokov, M. M.; Klimovskikh, I. I.; Bentmann, H.; Estyunin, D.; Zeugner, A.; Aliev, Z. S.; Gaß, S.; Wolter, A. U. B.; Koroleva, A. V.; Shikin, A. M.; et al. Prediction and observation of an antiferromagnetic topological insulator. *Nature* **2019**, *576*, 416−422.

(12) Cui, J.; Lei, B.; Shi, M.; Xiang, Z.; Wu, T.; Chen, X. H. Layer-dependent magnetic structure and anomalous Hall effect in the magnetic topological insulator $MnBi_4Te_7$. *Nano Lett.* **2023**, *23*, 1652−1658.

(13) Yang, S.; Xu, X.; Zhu, Y.; Niu, R.; Xu, C.; Peng, Y.; Cheng, X.; Jia, X.; Huang, Y.; Xu, X.; Lu, J.; Ye, Y. Odd-even layer-number effect and layer-dependent magnetic phase diagrams in $MnBi_2Te_4$. *Phys. Rev. X* **2021**, *11*, No. 011003.

(14) Otrokov, M. M.; Rusinov, I. P.; Blanco-Rey, M.; Hoffmann, M.; Vyazovskaya, A. Y.; Eremeev, S. V.; Ernst, A.; Echenique, P. M.; Arnau, A.; Chulkov, E. V. Unique thickness-dependent properties of the van der Waals interlayer antiferromagnet $MnBi_2Te_4$ films. *Phys. Rev. Lett.* **2019**, *122*, No. 107202.

(15) Ovchinnikov, D.; Huang, X.; Lin, Z.; Fei, Z.; Cai, J.; Song, T.; He, M.; Jiang, Q.; Wang, C.; Li, H.; Wang, Y.; Wu, Y.; Xiao, D.; Chu, J.-H.; Yan, J.; Chang, C.-Z.; Cui, Y.-T.; Xu, X. Intertwined topological and magnetic orders in atomically thin Chern insulator $MnBi_2Te_4$. *Nano Lett.* **2021**, *21*, 2544−2550.

(16) Qian, G.; Shi, M.; Chen, H.; Zhu, S.; Hu, J.; Huang, Z.; Huang, Y.; Chen, X.-H.; Gao, H.-J. Spin-flop transition and Zeeman effect of defect-localized bound states in the antiferromagnetic topological insulator $MnBi_2Te_4$. *Nano Res.* **2023**, *16*, 1101−1106.
(17) Hu, C.; Gordon, K. N.; Liu, P.; Liu, J.; Zhou, X.; Hao, P.; Narayan, D.; Emmanouilidou, E.; Sun, H.; Liu, Y.; Brawer, H.; Ramirez, A. P.; Ding, L.; Cao, H.; Liu, Q.; Dessau, D.; Ni, N. A van der Waals antiferromagnetic topological insulator with weak interlayer magnetic coupling. *Nat. Commun.* **2020**, *11*, 97.
(18) Gao, A.; Liu, Y.-F.; Qiu, J.-X.; Ghosh, B.; V. Trevisan, T.; Onishi, Y.; Hu, C.; Qian, T.; Tien, H.-J.; Chen, S.-W.; et al. Quantum metric nonlinear Hall effect in a topological antiferromagnetic heterostructure. *Science* **2023**, *381*, 181−186.
(19) Wang, N.; Kaplan, D.; Zhang, Z.; Holder, T.; Cao, N.; Wang, A.; Zhou, X.; Zhou, F.; Jiang, Z.; Zhang, C.; Ru, S.; Cai, H.; Watanabe, K.; Taniguchi, T.; Yan, B.; Gao, W. Quantum-metric-induced nonlinear transport in a topological antiferromagnet. *Nature* **2023**, *621*, 487−492.
(20) Kaplan, D.; Holder, T.; Yan, B. Unification of nonlinear anomalous Hall effect and nonreciprocal magnetoresistance in metals by the quantum geometry. *Phys. Rev. Lett.* **2024**, *132*, No. 026301.
(21) Gao, A.; Liu, Y.-F.; Hu, C.; Qiu, J.-X.; Tzschaschel, C.; Ghosh, B.; Ho, S.-C.; Bérubé, D.; Chen, R.; Sun, H.; et al. Layer Hall effect in a 2D topological axion antiferromagnet. *Nature* **2021**, *595*, 521−525.
(22) Zhang, Z.; Wang, N.; Cao, N.; Wang, A.; Zhou, X.; Watanabe, K.; Taniguchi, T.; Yan, B.; Gao, W. Controlled large non-reciprocal charge transport in an intrinsic magnetic topological insulator $MnBi_2Te_4$. *Nat. Commun.* **2022**, *13*, 6191.
(23) Liu, C.; Wang, Y.; Yang, M.; Mao, J.; Li, H.; Li, Y.; Li, J.; Zhu, H.; Wang, J.; Li, L.; et al. Magnetic-field-induced robust zero Hall plateau state in $MnBi_2Te_4$ Chern insulator. *Nat. Commun.* **2021**, *12*, 4647.
(24) Liu, C.; Wang, Y.; Li, H.; Wu, Y.; Li, Y.; Li, J.; He, K.; Xu, Y.; Zhang, J.; Wang, Y. Robust axion insulator and Chern insulator phases in a two-dimensional antiferromagnetic topological insulator. *Nat. Mater.* **2020**, *19*, 522−527.
(25) Gu, M.; Li, J.; Sun, H.; Zhao, Y.; Liu, C.; Liu, J.; Lu, H.; Liu, Q. Spectral signatures of the surface anomalous Hall effect in magnetic axion insulators. *Nat. Commun.* **2021**, *12*, 3524.
(26) Zhang, D.; Shi, M.; Zhu, T.; Xing, D.; Zhang, H.; Wang, J. Topological axion states in the magnetic insulator $MnBi_2Te_4$ with the quantized magnetoelectric effect. *Phys. Rev. Lett.* **2019**, *122*, No. 206401.
(27) Ge, J.; Liu, Y.; Li, J.; Li, H.; Luo, T.; Wu, Y.; Xu, Y.; Wang, J. High-Chern-number and high-temperature quantum Hall effect without Landau levels. *Natl. Sci. Rev.* **2020**, *7*, 1280−1287.
(28) Ying, Z.; Zhang, S.; Chen, B.; Jia, B.; Fei, F.; Zhang, M.; Zhang, H.; Wang, X.; Song, F. Experimental evidence for dissipationless transport of the chiral edge state of the high-field Chern insulator in $MnBi_2Te_4$ nanodevices. *Phys. Rev. B* **2022**, *105*, No. 085412.
(29) Gong, Y.; Guo, J.; Li, J.; Zhu, K.; Liao, M.; Liu, X.; Zhang, Q.; Gu, L.; Tang, L.; Feng, X.; et al. Experimental realization of an intrinsic magnetic topological insulator. *Chin. Phys. Lett.* **2019**, *36*, No. 076801.
(30) Zhao, Y.-F.; Zhou, L.-J.; Wang, F.; Wang, G.; Song, T.; Ovchinnikov, D.; Yi, H.; Mei, R.; Wang, K.; Chan, M. H. W.; et al. Even−odd layer-dependent anomalous Hall effect in topological magnet $MnBi_2Te_4$ thin films. *Nano Lett.* **2021**, *21*, 7691−7698.
(31) Zhu, K.; Bai, Y.; Hong, X.; Geng, Z.; Jiang, Y.; Liu, R.; Li, Y.; Shi, M.; Wang, L.; Li, W.; et al. Investigating and manipulating the molecular beam epitaxy growth kinetics of intrinsic magnetic topological insulator $MnBi_2Te_4$ with in situ angle-resolved photoemission spectroscopy. *J. Phys.: Condens. Matter* **2020**, *32*, No. 475002.
(32) Su, S.-H.; Chang, J.-T.; Chuang, P.-Y.; Tsai, M.-C.; Peng, Y.-W.; Lee, M. K.; Cheng, C.-M.; Huang, J.-C. A. Epitaxial growth and structural characterizations of $MnBi_2Te_4$ thin films in nanoscale. *Nanomaterials* **2021**, *11*, 3322.
(33) Xu, R.; Bai, Y.; Zhou, J.; Li, J.; Gu, X.; Qin, N.; Yin, Z.; Du, X.; Zhang, Q.; Zhao, W.; et al. Evolution of the electronic structure of ultrathin $MnBi_2Te_4$ films. *Nano Lett.* **2022**, *22*, 6320−6327.
(34) Zhu, K.; Cheng, Y.; Liao, M.; Chong, S. K.; Zhang, D.; He, K.; Wang, K. L.; Chang, K.; Deng, P. Unveiling the anomalous Hall response of the magnetic structure changes in the epitaxial $MnBi_2Te_4$ films. *Nano Lett.* **2024**, *24*, 2181−2187.
(35) Liu, S.; Yu, J.-X.; Zhang, E.; Li, Z.; Sun, Q.; Zhang, Y.; Cao, L.; Li, L.; Zhao, M.; Leng, P.; et al. Gate-tunable intrinsic anomalous Hall effect in epitaxial $MnBi_2Te_4$ films. *Nano Lett.* **2024**, *24*, 16−25.
(36) Bai, Y.; Li, Y.; Luan, J.; Liu, R.; Song, W.; Chen, Y.; Ji, P.-F.; Zhang, Q.; Meng, F.; Tong, B.; et al. Quantized anomalous Hall resistivity achieved in molecular beam epitaxy-grown $MnBi_2Te_4$ thin films. *Natl. Sci. Rev.* **2024**, *11*, No. nwad189.
(37) Luo, J.; Tong, Q.; Jiang, Z.; Bai, H.; Wu, J.; Liu, X.; Xie, S.; Ge, H.; Zhao, Y.; Liu, Y.; et al. Exploring the epitaxial growth kinetics and anomalous Hall effect in magnetic topological insulator $MnBi_2Te_4$ films. *ACS Nano* **2023**, *17*, 19022−19032.
(38) Cai, Z.; Liu, B.; Zou, X.; Cheng, H.-M. Chemical vapor deposition growth and applications of two-dimensional materials and their heterostructures. *Chem. Rev.* **2018**, *118*, 6091−6133.
(39) Zhou, J.; Lin, J.; Huang, X.; Zhou, Y.; Chen, Y.; Xia, J.; Wang, H.; Xie, Y.; Yu, H.; Lei, J.; et al. A library of atomically thin metal chalcogenides. *Nature* **2018**, *556*, 355−359.
(40) Zhang, Y.; Yao, Y.; Sendeku, M. G.; Yin, L.; Zhan, X.; Wang, F.; Wang, Z.; He, J. Recent Progress in CVD growth of 2D transition metal dichalcogenides and related heterostructures. *Adv. Mater.* **2019**, *31*, No. 1901694.
(41) Li, J.; Chen, M.; Zhang, C.; Dong, H.; Lin, W.; Zhuang, P.; Wen, Y.; Tian, B.; Cai, W.; Zhang, X. Fractal-theory-based control of the shape and quality of CVD-grown 2D materials. *Adv. Mater.* **2019**, *31*, No. 1902431.
(42) Wu, J.; Liu, F.; Liu, C.; Wang, Y.; Li, C.; Lu, Y.; Matsuishi, S.; Hosono, H. Toward 2D magnets in the $(MnBi_2Te_4)(Bi_2Te_3)_n$ bulk crystal. *Adv. Mater.* **2020**, *32*, No. 2001815.
(43) Klimovskikh, I. I.; Otrokov, M. M.; Estyunin, D.; Eremeev, S. V.; Filnov, S. O.; Koroleva, A.; Shevchenko, E.; Voroshnin, V.; Rybkin, A. G.; Rusinov, I. P.; et al. Tunable 3D/2D magnetism in the $(MnBi_2Te_4)(Bi_2Te_3)_m$ topological insulators family. *npj Quantum Mater.* **2020**, *5*, 54.
(44) Zhou, J.; Zhu, C.; Zhou, Y.; Dong, J.; Li, P.; Zhang, Z.; Wang, Z.; Lin, Y.-C.; Shi, J.; Zhang, R.; et al. Composition and phase engineering of metal chalcogenides and phosphorous chalcogenides. *Nat. Mater.* **2023**, *22*, 450−458.
(45) Choe, J.; Lujan, D.; Rodriguez-Vega, M.; Ye, Z.; Leonardo, A.; Quan, J.; Nunley, T. N.; Chang, L.-J.; Lee, S.-F.; Yan, J.; et al. Electron−phonon and spin−lattice coupling in atomically thin layers of $MnBi_2Te_4$. *Nano Lett.* **2021**, *21*, 6139−6145.
(46) Liu, Y.; Tang, M.; Meng, M.; Wang, M.; Wu, J.; Yin, J.; Zhou, Y.; Guo, Y.; Tan, C.; Dang, W.; et al. Epitaxial growth of ternary topological insulator Bi_2Te_2Se 2D crystals on mica. *Small.* **2017**, *13*, No. 1603572.
(47) Yin, L.; Cheng, R.; Wen, Y.; Zhai, B.; Jiang, J.; Wang, H.; Liu, C.; He, J. High-performance memristors based on ultrathin 2D copper chalcogenides. *Adv. Mater.* **2022**, *34*, No. 2108313.
(48) Bian, M.; Zhu, L.; Wang, X.; Choi, J.; Chopdekar, R.; Wei, S.; Wu, L.; Huai, C.; Marga, A.; Yang, Q.; et al. Dative epitaxy of commensurate monocrystalline covalent van der Waals moiré supercrystal. *Adv. Mater.* **2022**, *34*, No. 2200117.

https://doi.org/10.1021/acs.nanolett.4c04700
Nano Lett. 2024, 24, 15788−15795